

Investigation of infrasound signatures from microbaroms using OH airglow and ground-based microbarometers

Thurian Le Du, Pierre Simoneau, Philippe Keckhut, Alain Hauchecorne, Alexis Le Pichon

▶ **To cite this version:**

Thurian Le Du, Pierre Simoneau, Philippe Keckhut, Alain Hauchecorne, Alexis Le Pichon. Investigation of infrasound signatures from microbaroms using OH airglow and ground-based microbarometers. Advances in Space Research, 2020, 65 (3), pp.902-908. 10.1016/j.asr.2019.11.026 . insu-02405801

HAL Id: insu-02405801
https://insu.hal.science/insu-02405801

Submitted on 6 Jan 2020

HAL is a multi-disciplinary open access archive for the deposit and dissemination of scientific research documents, whether they are published or not. The documents may come from teaching and research institutions in France or abroad, or from public or private research centers.

L'archive ouverte pluridisciplinaire **HAL**, est destinée au dépôt et à la diffusion de documents scientifiques de niveau recherche, publiés ou non, émanant des établissements d'enseignement et de recherche français ou étrangers, des laboratoires publics ou privés.

Available online at www.sciencedirect.com

ScienceDirect

Advances in Space Research xxx (2019) xxx–xxx

ADVANCES IN SPACE RESEARCH (a COSPAR publication)

www.elsevier.com/locate/asr

Investigation of infrasound signatures from microbaroms using OH airglow and ground-based microbarometers

Thurian Le Dû [a,b,*], Pierre Simoneau [a], Philippe Keckhut [b], Alain Hauchecorne [b], Alexis Le Pichon [c]

[a] ONERA, Chemin de la Huniére, F- 91761 Palaiseau, France
[b] LATMOS/IPSL, UVSQ Université Paris-Saclay, Sorbonne Université, CNRS, Guyancourt, France
[c] CEA, DAM, DIF, Arpajon, France

Received 6 September 2019; received in revised form 7 November 2019; accepted 19 November 2019

Abstract

In the frame of the European H2020 project ARISE, a short wave infrared (SWIR) InGaAs camera has been operated at the Haute-Provence Observatory, during a night that corresponds to the peak of Geminid meteor shower to investigate infrasound associated with meteor arrivals. This camera allows continuous observations during clear-sky nighttime of the OH airglow layer centered at 87 km. These observations were collocated with Rayleigh lidar measurements providing vertical temperature profiles from the lower stratosphere to the altitude of the OH layer around the mesopause. Spectral analysis of OH images did not allow to detect infrasound associated with meteor trails, however it reveals a peak corresponding to infrasound signals in the frequency band of those produced by ocean swell. Infrasound wave activity observed from ground-based microbarometers as well as the OH camera, appear to be modified with the presence of a temperature inversion described by Rayleigh lidar. Indeed, there is a difference in energy related to infrasonic activity between the first part of the night during the temperature inversion and after the inversion.
© 2019 COSPAR. Published by Elsevier Ltd. This is an open access article under the CC BY license (http://creativecommons.org/licenses/by/4.0/).

Keywords: OH; Infrasound; Airglow; Microbaroms

1. Introduction

Infrasonic waves are sub-audible sound waves with frequencies below 20 Hz down to 0.003 Hz. The last one corresponds to the Brunt-Väisälä frequency. Their sources are multiple and can be anthropogenic or natural such as volcanic activity, earthquakes, aurora, severe weather and man-made explosions. These low-frequency waves propagate easily in many media including the atmosphere. Infrasounds emitted at ground level, propagate vertically up to the upper mesosphere and are partly refracted on the different layers of the atmosphere leading to a downward propagation with a part propagating upward to the thermosphere (Waxler and Assink, 2019). A global network of microbarometers is being deployed within the CTBTO (Preparatory commission for the Comprehensive Nuclear-Test-Ban Treaty Organization) framework to detect any nuclear explosion. Such sensors are sensitive to all sort of sources of infrasounds while their propagation are modified during their transit into the atmosphere and are then sensitive to wind and temperature fluctuations (LePichon et al., 2018).

When meteors enters the atmosphere at a speed (typically 20 km/s) they produce a streak of light corresponding

* Corresponding author at: ONERA, Chemin de la Huniére, F- 91761 Palaiseau, France.
E-mail addresses: thurian.le_du@onera.fr (T. Le Dû), pierre.simoneau@onera.fr (P. Simoneau), Philippe.Keckhut@latmos.ipsl.fr (P. Keckhut), Alain.hauchecorne@latmos.ipsl.fr (A. Hauchecorne), Alexis.LEPICHON@CEA.FR (A.L. Pichon).

https://doi.org/10.1016/j.asr.2019.11.026
0273-1177/© 2019 COSPAR. Published by Elsevier Ltd.
This is an open access article under the CC BY license (http://creativecommons.org/licenses/by/4.0/).

Please cite this article as: T. Le Dû, P. Simoneau, P. Keckhut et al., Investigation of infrasound signatures from microbaroms using OH airglow and ground-based microbarometers, Advances in Space Research, https://doi.org/10.1016/j.asr.2019.11.026

to the aerodynamic heating, well known as "shooting star" but also prior to its ablation, infrasounds are produced during their interaction with atmosphere. Microbarometers have already recorded infrasound emitted by the explosive fragmentation of the 2013 Chelyabinsk meteorite and others, which made it possible to study long range propagation effects (Pilger et al., 2015). However, the entry of small meteors into the atmosphere is not the main source of infrasound, and often overlap with other continuous source of infrasound like the ocean swell. The ARISE (Atmospheric dynamics Research InfraStructure in Europe) project focuses on atmospheric dynamics of the middle atmosphere which integrates the stratosphere and mesosphere, use a set of different techniques including the infrasound technology for a better understanding of dynamical processes (Blanc et al., 2018). One of the techniques used in the ARISE project is the observation of nightglow radiation.

Nightglow radiation, also known as airglow, takes its sources mainly in the emission lines photochemically produced by atoms and molecules like, for example, OH, O2 and atomic oxygen. Nightglow emissions from OH and O2 molecule dominate the terrestrial radiation in the short wavelength infrared (SWIR) region (Meinel, 1950; Rousselot et al., 2000). Airglow is a sensitive indicator of the changes in chemical composition, temperature and dynamics prevailing near the emitting region (Faivre et al., 2003; Bellisario et al., 2019; Smith, 2004). Imaging observations have been successfully used to study horizontal structures associated with dynamical forcings like gravity waves at different scales (Abreu and Yee, 1989; Fritts et al., 2009). In this study, OH radiation has been choosen because it is the most intense in the SWIR band allowing high frame rate acquisition (typically 500 to 1000 ms) by our imaging system. Some articles deal with the theoretical propagation of infrasound to the OH layer (Snively, 2013).

In order to study infrasonic waves associated with the meteor activity or arrival, an airglow campaign was carried out on December 2017 at the Haute-Provence Observatory (OHP). This period corresponds to the peak activity of Gemenid meteor shower during three to four nights thereby allowing detection of infrasonic signatures from supersonic meteors. Among the three nights of observation, December 12th was the only cloud-free night, which is necessary for the observation of OH radiation. Other studies have analyzed the OH temperature modulations caused by the propagation of infrasound with periods of several minutes using the GRIPS (GRound-based Infrared P-branch Spectrometer) measurement system (Bittner et al., 2010; Pilger and Bittner, 2009) but the present study is about the perturbation of OH radiation caused by the propagation of infrasound with periods of a few seconds using a short-wave infrared camera.

Moreover, during this campaign, a mesospheric inversion inducing a large temperature disturbance was present, allowing to provide preliminary results about the influence of the mesospheric state on infrasound propagation.

2. Description of the instruments

Short-wave infrared (SWIR) camera was placed at the Haute-Provence Observatory to measure the nightglow radiation emitted by OH at an altitude of 87 km. OHP is equipped with many instruments, including a Rayleigh lidar to measure the temperature and microbarometers to measure amplitude infrasound signals.

2.1. Nightglow measurements

A SWIR camera based on a thermoelectric cooled InGaAs detector (640 × 512 pixels, pitch 25 μm) has been used during the two campaigns. The spectral bandwidth of the camera ranges from 0.9 to 1.7 μm. This bandwidth corresponds to vibrational transitions $\Delta v = 2$ and 3 of the OH Meinel band system. The integration time used for present investigation is 400 ms with a frame rate of 500 ms. Thus, for a whole night we acquire roughly 50000 images. A 12,5 mm focal lens was mounted on the camera giving a 32° × 27° field of view (FOV) which leads to a 111 × 89 km area observation at the OH layer level (~87 km) for a zenith viewing and an instantaneous field of view of 2 mrad leading to a spatial resolution of 174 meters at the OH layer altitude. The camera is radiometrically calibrated in laboratory leading to absolute integrated radiance measurements (in photons/s/m^2/sr). The acquired raw images are finally unwarpped and calibrated without any spatial treatment (no star removal,...) in order to avoid any loss of details.

2.2. Lidar Temperature profile measurement

Lidar temperature profiles are derived from molecular backscattering from laser pulses send vertically. Such method has been developed at OHP (Hauchecorne and Chanin, 1980) and has been operating regularly since 1979 providing the historical record. This method allows to study many processes occurring in the middle atmosphere including the detection of the cooling associated with greenhouse gases increase and ozone decrease (Keckhut et al., 1995). Such observations are validated through systematic comparisons (Keckhut et al., 2004). The accuracy obtained is linked with the statistical noise that increases with altitude and leads to a measurement smaller than 1 K below 70 km. Laser power and telescope size are critical parameters while vertical and time resolution can be degraded to improve the accuracy. In this study the vertical resolution corresponds to 75 meters and the time average is equal to 5 min.

2.3. Microbarometers measurements

Microbarom signals, generated by the non-linear interaction of ocean gravity waves at the ocean surface dominate the infrasound background noise between 0.1 and 0.5 Hz (Longuet-Higgins, 1950; Hupe et al., 2018). These signals are globally and permanently detected by

Please cite this article as: T. Le Dû, P. Simoneau, P. Keckhut et al., Investigation of infrasound signatures from microbaroms using OH airglow and ground-based microbarometers, Advances in Space Research, https://doi.org/10.1016/j.asr.2019.11.026

the International Monitoring System (IMS) infrasound network, which was established to monitor compliance with the Comprehensive Nuclear-Test-Ban Treaty (Ceranna et al., 2019). Measuring microbaroms using sensitive acoustic antenna provides useful integrated information about the stratospheric wind dynamics with high temporal resolution (Pichon et al., 2015). Motivated by these studies, one experimental four-element array of ~3 km aperture has been installed at OHP, collocated to the lidar station, to further explore atmospheric remote sensing methods using near-continuous signals. To obtain infrasound detection results, continuous infrasound recordings are processed by implementing the progressive multichannel correlation (PMCC) algorithm (Cansi, 1995). By applying the PMCC algorithm, all coherent infrasonic signals are detected and their wave parameters are estimated in the frequency range of 0.05–5 Hz. In this band, 15 logscaled frequency bandwidths with a window length linearly scaled to the period are used to better discriminate between interfering signals (Matoza et al., 2013). During normal winter conditions, microbaroms with a mean frequency of ~0.25 Hz are continuously detected and dominate westerly from the Atlantic ocean as we can observe on Fig. 1, which is a wavelet analysis of the pressure profile measured during the night of the 12–13 December.

3. Observations and results

In this section, we present the results of the observation campaign performed at the OHP in the south of France during the night of the December 12th-13th 2017. During this campaign, three nights of measurements were made but only one night had sky without clouds and rain and this night was the only one where the lidar sounding was done. Fig. 2 shows an example of image acquired from this night, we can observe gravity waves with an horizontal wavelength around 20 km modifying the emitted radiation.

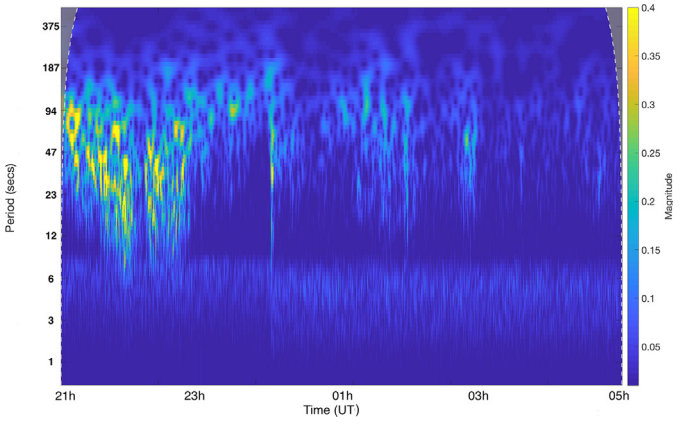


Fig. 1. Wavelet analysis of the pressure profile measured by the sensitive microbarometer during the night of the 12–13 December at OHP. The magnitude band centered on 0.25 Hz is visible at the bottom of the figure.

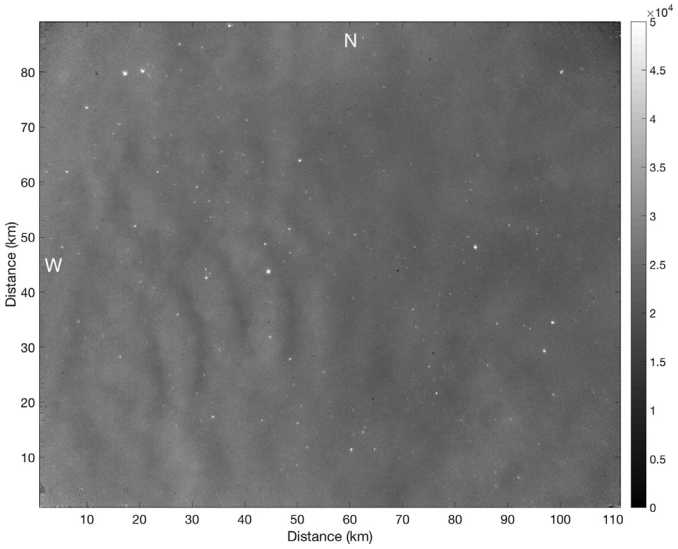


Fig. 2. Raw image of the OH radiation at altitude 87 km during the night of the 12–13 December 2017. The radiance scale is in ph/s/m^2/sr.

The analysis of the images allows the determination of the temporal evolution of the mean radiance during the whole night. In order to reduce signal noise, a matrix of five by five pixels is selected in the center of each image and their average is computed to get the OH radiance temporal profile (Fig. 3a). In our images we observe the apparent velocity of the infrasound on the horizontal OH layer, it is equal to:

$$v_{OH} = \frac{v_s}{\sin\theta} \quad (1)$$

with θ the angle between the propagation direction and the vertical and v_s the sound speed at the OH layer altitude (~ 270 m/s). Thus, the apparent velocity of the waves with a small theta will be greater than the theoretical velocity of sound at the OH layer. For example, infrasound can be reflected at the thermosphere and reaches the OH layer with oblique propagation. Five pixels represent 870 m, so the Nyquist limit is set at 1740 m. The corresponding phase velocity with a wavelength of 1740 meters and a period of 3 s is 580 m/s. With this value we can calculate the corresponding theta angle which is 28 degrees. For example, by using a five by five pixels matrix, for the case of waves with a three-second period, incidence angles greater than 28 degrees are filtered. In addition, the apparent speed of infrasound may be increased due to wind conditions.

We are now able to compute the temporal evolution of the radiance along the night using these matrix. Then, a spectral analysis is performed to determine the frequency content of the night using this radiance temporal profile. For this purpose, a Morlet wavelet transform is used as well as power spectral density (Matlab code). These tools are complementary and are used to characterize the infrasonic activity of the night. The Morlet wavelet analysis allow to compute the time–frequency representation of the radiance temporal profile in order to calculate wavelet

Please cite this article as: T. Le Dû, P. Simoneau, P. Keckhut et al., Investigation of infrasound signatures from microbaroms using OH airglow and ground-based microbarometers, Advances in Space Research, https://doi.org/10.1016/j.asr.2019.11.026

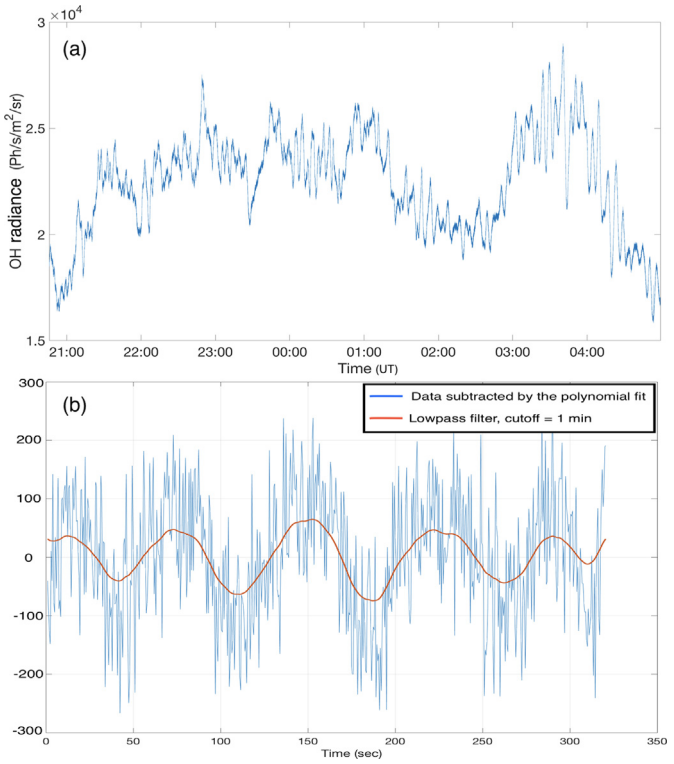


Fig. 3. (a): Temporal OH radiance profile of the 12–13 December at the OHP. (b): Portion of the OH radiance profile at the beginning of the night smoothed by applying a lowpass filter with a one minute cutoff period (red line). A dominant oscillation of ~75 s is noted.

magnitude and locate the detected frequencies in time. Power spectral densities calculations are independent measures of these frequencies.

During the whole night, the camera acquired images with a frame rate of 500 ms towards the zenith. From the 54 000 images acquired, a profile of the OH radiance is obtained as a function of time (Fig. 3a). Oscillations are observed with periods longer than the Brunt-Väisälä frequency (characteristics of gravity waves) but also periods of few seconds. In order to visualize these periods, a portion at the beginning of this profile has been smoothed to better visualize the amplitude and frequency of the variation on the radiance profile (Fig. 3b). A three order polynomial fit was subtracted from the records. The red curve is the result of a first order Butterworth lowpass filter with a 1/60 cut-off frequency. This filtering highlights a 75 s period. Therefore it seems that the radiation emitted by OH can be disturbed by periods below the Brunt-Väisälä period (~ 5 min) which corresponds to the frequency range of infrasound. This oscillation is confirmed by the wavelet analysis of the radiance temporal profile at this time.

The oscillations were not correlated with meteor arrivals and the spectral analysis has not allowed to clearly identify infrasound sources associated with meteor trails in the thermosphere. Moreover, the too wide frequency range of infrasound generated by meteors (0.01–20 Hz) makes it difficult to identify them. Furthermore, the previous analysis concerns a small part of the image. The analysis of the entire image, except for the edges that are elongated by the camera, would allows us to etablish a statistic for the observed periods. As before, the radiance temporal profile is calculated for each pixel, but for a temporal window of 40 s, in order to detect only one perturbation at a time. The wavelet transform of each radiance profile is computed between 3 and 10 s. From this treatment, we can detect the frequency and the onset time of the signals which magnitude is greater than a given threshold value (set to 3/4 of the maximum magnitude of the wavelet transform), in order to detect strong signal perturbations above the camera noise. A time equal to zero (dark blue in the color scale) at a given pixel means that there have been no disturbances whose magnitude is greater than the threshold at that pixel during the 40 s. The speed of these perturbations can be calculated because the distance between the pixels and the onset time of the perturbation at each pixel are known. This treatment give a map of perturbations propagations, some of them is propagating at the speed of sound. Fig. 4, which is a part of the previous map, shows a color gradient resulting in the propagation of such perturbation with an apparent horizontal speed of 430 m/s as well as the associated propagation direction represented by the red arrow. The white two-way arrow shows a distance between two pixels of 1722 meters and the two one-way arrows show the onset time of these pixels, necessary for calculating the horizontal speed of the perturbation in this case. This detected wave are consistent with dominant source region of microbaroms from south of Greenland detected by the colocated infrasound array. A statistical study was conducted for the determination of a dominant direction over the entire image field but was inconclusive. The study revealed other propagations with lower speeds, probably

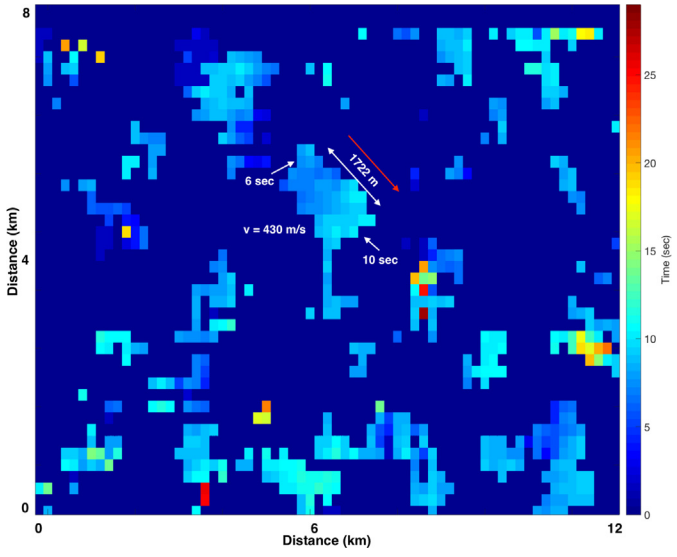


Fig. 4. Part of the image showing an example of detected perturbation. The example show a perturbation propagation at the sound speed with a 5 s period. The direction of propagation is manually deduced by following the color gradient and shown by the red arrow, consistent with waves originating from the northwestern.

Please cite this article as: T. Le Dû, P. Simoneau, P. Keckhut et al., Investigation of infrasound signatures from microbaroms using OH airglow and ground-based microbarometers, Advances in Space Research, https://doi.org/10.1016/j.asr.2019.11.026

disturbances caused by turbulence. The histogram of the periods associated with each detection between 3 and 10 s shows a distribution centered on 5 s (Fig. 5), which corresponds to the period of dominant microbaroms (Fig. 1).

To confirm this finding, the radiance temporal profile corresponding to the first 42 min of the night has been divided into 5 segments. Each of them were filtered by applying a first order Butterworth high-pass filter removing periods above 30 s and a 20% cosine taper was applied to reduce discontinuities in the fourier transform. The power spectral density (psd) was calculated for each segment and then summed. This method was applied and summed 300 times by taking random positions in the images. A moving average was applied to the result for more visibility. The result shows a net increase in power between 3 and 6 s. This increase is reflected in looking at other times of the night.

4. Impact of the mesospheric temperature inversion on wave propagation

4.1. Airglow image analysis

Along the night, temperature profiles were acquired using the OHP's Rayleigh lidar. The profile shows a strong temperature inversion at the beginning of the night at an altitude of 65 km and then disappears around midnight as shown in Fig. 6. Mesospheric temperature inversions correspond to the largest perturbation in the mesosphere that can exhibit a temperature increase of 20 to 40 K (Hauchecorne et al., 1987) over several kilometers vertically. Their occurrence is most probably due to gravity wave breaking as simulated by numerical models (Maillard et al., 1990). Lidar observations reveal the presence of a strong westerly mesospheric jet in the winter hemisphere at mid-latitude which favors the vertical propagation of gravity waves. Associated instabilities lead to slow down the wind and invert the temperature gradient for several consecutive days. It is interesting to look at the effect of this inversion on the waves propagation with periods of a few seconds. The OH radiance temporal profile before and after the temperature inversion were analysed independantly.

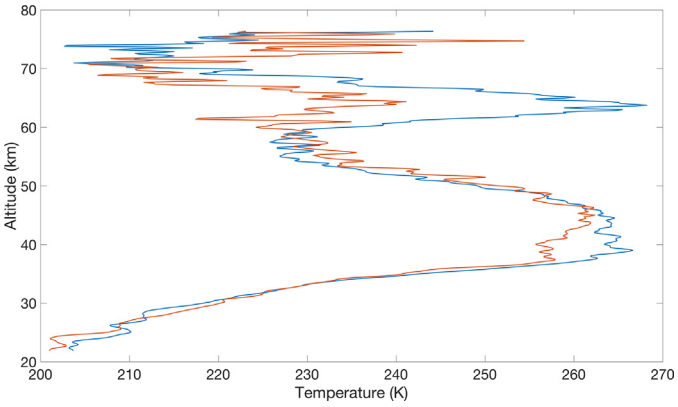


Fig. 6. Rayleigh lidar temperature profiles. The blue curve represents the average temperature for each altitude during the temperature inversion and the red curve is the average temperature after the inversion.

The power spectral density of both parts (before and after the end of the inversion) will highlight differents frequency ranges. Each part is divided into 20 segments of 11 min each. The power spectral density is calculated for each segment. They are summed to reduce noise and the two resulting power spectral densities are divided between them. The result is shown in Fig. 7. The blue curve is the psd of the first part divided by the psd of the second part, and conversely for the red curve, then a sliding average is applied to the result to improve visibility. The same calculation was performed on a noise profile from the camera to confirm our result are not induced by the acquisition noise. It should be noted that the first part of the night has more energy in the 3–100 s range than the second part. It can therefore be assumed that temperature inversion would increase infrasonic activity up to 87 km altitude. However, wind must also be known to more accurately quantify the impact of inversion on wave propagation.

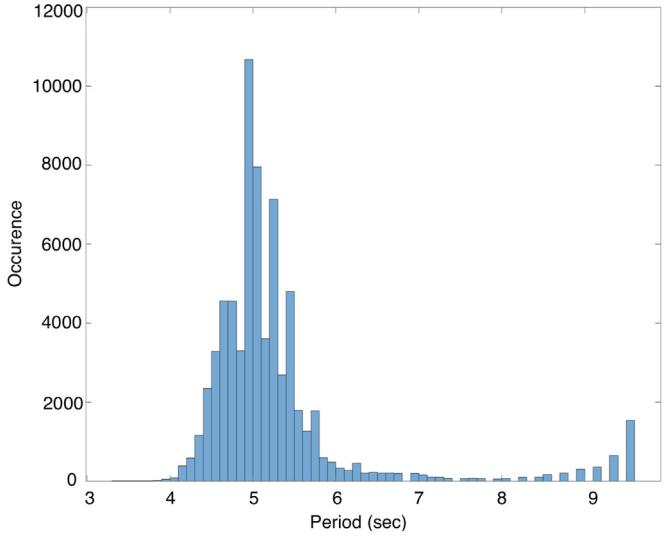


Fig. 5. Histogram of the periods detected over the entire image. The distribution is centered on 5 s.

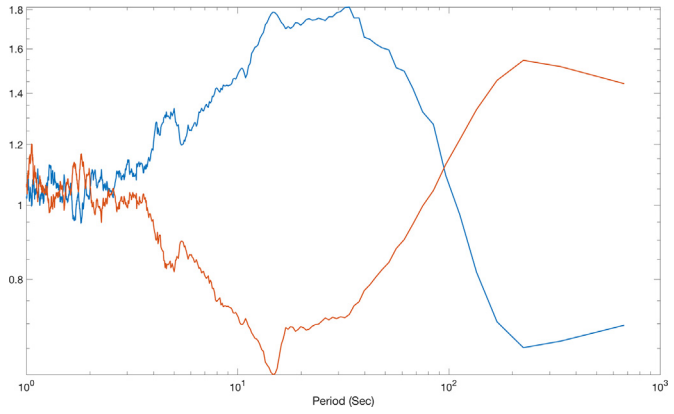


Fig. 7. The blue curve is the power ratio between the first part and the second part of the night and vice versa for the red curve.

Please cite this article as: T. Le Dû, P. Simoneau, P. Keckhut et al., Investigation of infrasound signatures from microbaroms using OH airglow and ground-based microbarometers, Advances in Space Research, https://doi.org/10.1016/j.asr.2019.11.026

In order to deduce the exact time at which the frequency range 10–100 s experiences a decrease in energy, the average magnitude of the power spectral density for each of the 40 segments between 10 and 100 s during the night is calculated. The result tends to decrease with time which reinforces the hypothesis that the inversion plays a role in the decrease of infrasound energy with time.

4.2. Microbarometer measurements

Ground-based microbarometers have measured pressure fluctuations caused by the propagation of infrasound and allow the propagation direction and frequency of infrasound to be deduced using the PMCC algorithm. A Morlet wavelet analysis of the radiance temporal profile was calculated between 0.1 and 0.01 Hz and confirms that there is an increase in magnitude at the beginning of the night and then disappeared around 1am (Fig. 8a). A similar analysis of the pressure profile measured at ground level reveals the same behaviour but the increase in magnitude ends earlier, at around 23:30 UT (Fig. 8b). The same behaviour both on the ground and at 87 km altitude is observed. That part of the infrasound may be reflected by the temperature inversion and can be trapped between the altitude of the inversion ($\sim$ 65 km) and the OH layer and between 65 km and the ground. This cause an increase of the infrasound activity at the beginning of the night. The opposite effect concerning microbaroms is noticed. The magnitude of the wavelet analysis between 2 and 6 s of the pressure profile measured by the microbarometers (Fig. 1) is divided into 144 parts and these parts are averaged. The magnitude in the band 2–6 s seems to be weaker during the inversion than after. The change is observable at midnight, when the temperature inversion disappears. This may be due to the trapping of infrasound above the temperature inversion and can thus not reach the ground, which it does when the temperature inversion dissolves. The result is shown in Fig. 9. Concerning the OH layer, if we look at Fig. 7, we can see that there is a peak centered on 5 s on the blue curve. This means that the infrasound generated by the ocean swell is stronger at the beginning of the night than at the end of the night, which is consistent with the results on the ground.

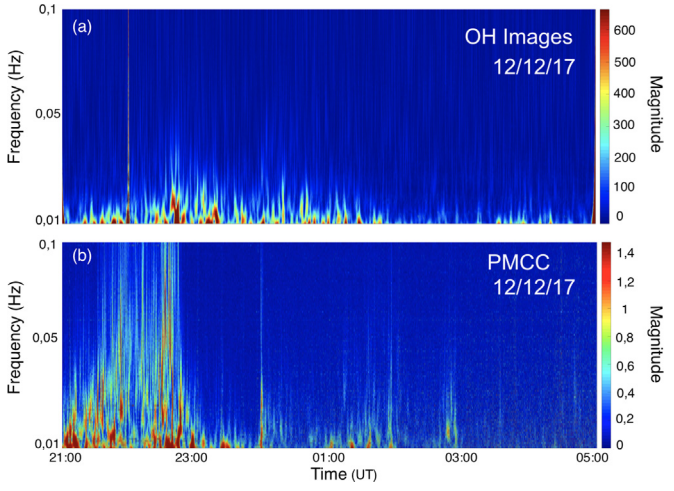


Fig. 8. (a): Wavelet transform of the OH radiance profile between 0,1 and 0,01 Hz for the entire night. (b): Wavelet transform of the pressure profile measured at ground with microsensors.

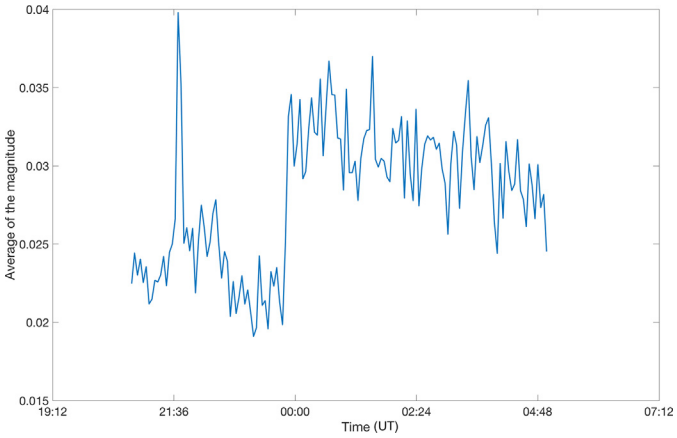


Fig. 9. Average of the magnitude of the pressure profile divided into 144 parts in the range [2–6] seconds.

5. Discussion and concluding remarks

In this work we have shown that the radiation emitted by the OH molecule can be disturbed by the propagation of perturbations of the order of few seconds, in particular infrasound generated by ocean swells that have a specific frequency signature around 0.2 Hz. Nevertheless it seems we were not able to detect infrasounds generated by meteor trails. It has also been shown that the particular temperature profile of the night of December 12th 2017 plays a role in modifying infrasonic activity during the night by simultaneously observing this activity on the ground and at 87 km altitude.

A sensitivity test with a numerical model reproducing the intensity of Nightglow radiation must be carried out in order to theoretically verify that the infrasound passage disturbs Nightglow radiation. In addition, further work is needed to verify if the infrasonic signature of the ocean swell is found on other nights and thus consolidate the results of this study.

In addition, this study may be a first step in using Nightglow radiation perturbation by infrasound propagation to infer local physical parameters such as wind speed and direction, which would allow us to better understand the dynamic processes occurring in the upper mesosphere.

This study proposes an original approach for infrasound detection because airglow observations has been fewly used in this respect. Pilger et al. (2013) used airglow deduced temperature temporal evolution to detect the passage of infrasound with periods in the order of few minutes and a modeling work to identify sources was carried out. Our work directly use the intensity of the emitted airglow and

Please cite this article as: T. Le Dû, P. Simoneau, P. Keckhut et al., Investigation of infrasound signatures from microbaroms using OH airglow and ground-based microbarometers, Advances in Space Research, https://doi.org/10.1016/j.asr.2019.11.026

has made it possible to detect infrasound with periods in the order of few seconds while identifying the source (ocean swell) from the images. Moreover, the observation of the impact of temperature inversion on infrasonic activity is an interesting result for a better understanding of sound wave propagation in the atmosphere.

Declaration of Competing Interest

The authors declare that they have no known competing financial interests or personal relationships that could have appeared to influence the work reported in this paper.

Acknowledgements

This work was performed during the course of the ARISE design study (http://arise-project.eu) funded by the European Union's Horizon 2020 Research and Innovation Program under Grant Agreement No. 653980. The colleagues from the Observatory of Paris have also participated to the campaign. The authors are also grateful to the Observatory of Haute-Provence and LATMOS staff who run the lidar within the NDACC network, facility supported by INSU/CNRS and CNES.

References

Abreu, V.J., Yee, J., 1989. Diurnal and seasonal variation of the nighttime OH (8–3) emission at low latitudes. J. Geophys. Res.: Space Phys. 94 (A9), 11949–11957. https://doi.org/10.1029/JA094iA09p11949.

Bellisario, C., Hauchecorne, A., Simoneau, P., Keckhut, P., 2019. 'Modelling of the nightglow radiation for comparisons with surface observations. J. Space Weather Space Climate (submitted for publication).

Bittner, M., Höppner, K., Pilger, C., Schmidt, C., 2010. Mesopause temperature perturbations caused by infrasonic waves as a potential indicator for the detection of tsunamis and other geo-hazards. Natural Hazards Earth Syst. Sci. 10 (7), 1431–1442. https://doi.org/10.5194/nhess-10-1431-2010.

Blanc, E., Ceranna, L., Hauchecorne, A., Charlton-Perez, A., Marchetti, E., Evers, L.G., Kvaerna, T., Lastovicka, J., Eliasson, L., Crosby, N. B., et al., 2018. Toward an improved representation of middle atmospheric dynamics thanks to the arise project. Surv. Geophys. 39 (2), 171–225. https://doi.org/10.1007/s10712-017-9444-0.

Cansi, Y., 1995. An automatic seismic event processing for detection and location: The pmcc method. Geophys. Res. Lett. 22 (9), 1021–1024. https://doi.org/10.1029/95GL00468.

Ceranna, L., Matoza, R., Hupe, P., Le Pichon, A., Landès, M., 2019. Systematic array processing of a decade of global ims infrasound data. In: Infrasound Monitoring for Atmospheric Studies. Springer, pp. 471–482. https://doi.org/10.1007/978-3-319-75140-5_13.

Faivre, M., Moreels, G., Pautet, D., Keckhut, P., Hauchecorne, A., 2003. Correlated measurements of mesospheric density and near infrared airglow. Adv. Space Res. 32 (5), 777–782. https://doi.org/10.1016/S0273-1177(03)00423-X.

Fritts, D., Abdu, M., Batista, B., Batista, I., Batista, P., Buriti, R., Clemesha, B., Dautermann, T., de Paula, E., Fechine, B. et al., 2009. The spread f experiment (spreadfex): Overview and summary of the spread f experiment (spreadfex), 27(11), 2141. URL: https://doi.org/10.5194/angeo-27-2141-2009.

Hauchecorne, A., Chanin, M.-L., 1980. Density and temperature profiles obtained by lidar between 35 and 70 km. Geophys. Res. Lett. 7 (8), 565–568. https://doi.org/10.1029/GL007i008p00565.

Hauchecorne, A., Chanin, M.L., Wilson, R., 1987. Mesospheric temperature inversion and gravity wave breaking. Geophys. Res. Lett. 14 (9), 933–936. https://doi.org/10.1029/GL014i009p00933.

Hupe, P., Ceranna, L., Pilger, C., de Carlo, M., Le Pichon, A., Kaifler, B., Rapp, M., 2018. Assessing middle atmosphere weather models using infrasound detections from microbaroms. Geophys. J. Int. 216 (3), 1761–1767. https://doi.org/10.1093/gji/ggy520.

Keckhut, P., Hauchecorne, A., Chanin, M., 1995. Midlatitude long-term variability of the middle atmosphere: Trends and cyclic and episodic changes. J. Geophys. Res.: Atmosph. 100 (D9), 18887–18897. https://doi.org/10.1029/95JD01387.

Keckhut, P., McDermid, S., Swart, D., McGee, T., Godin-Beekmann, S., Adriani, A., Barnes, J., Baray, J.-L., Bencherif, H., Claude, H., et al., 2004. Review of ozone and temperature lidar validations performed within the framework of the network for the detection of stratospheric change. J. Environ. Monit. 6 (9), 721–733. https://doi.org/10.1039/b404256e.

Le Pichon, A., Assink, J., Heinrich, P., Blanc, E., Charlton-Perez, A., Lee, C.F., Keckhut, P., Hauchecorne, A., Rüfenacht, R., Kämpfer, N., et al., 2015. Comparison of co-located independent ground-based middle atmospheric wind and temperature measurements with numerical weather prediction models. J. Geophys. Res.: Atmosp. 120 (16), 8318–8331. https://doi.org/10.1002/2015JD023273.

LePichon, A., Blanc, E., Hauchecorne, A., 2018. Infrasound Monitoring for Atmospheric Studies: Challenges and New Perspectives. Springer. https://doi.org/10.1007/978-3-319-75140-5.

Longuet-Higgins, M.S., 1950. A theory of the origin of microseisms. Philosoph. Trans. Roy. Soc. London. Series A, Mathe. Phys. Sci. 243 (857), 1–35. https://doi.org/10.1098/rsta.1950.0012.

Maillard, A., Hauchecorne, A., Rose, K., 1990. Planetary waves modulated by the quasi-biennial oscillation (qbo). Ann. Geophys. 8, 531–540.

Matoza, R.S., Landès, M., Le Pichon, A., Ceranna, L., Brown, D., 2013. Coherent ambient infrasound recorded by the international monitoring system. Geophys. Res. Lett. 40 (2), 429–433. https://doi.org/10.1029/2012GL054329.

Meinel, I., 1950. OH emission bands in the spectrum of the night sky. Astrophys. J. 111, 555. https://doi.org/10.1086/145296.

Pilger, C., Bittner, M., 2009. Infrasound from tropospheric sources: Impact on mesopause temperature? J. Atmos. Solar Terr. Phys. 71 (8–9), 816–822. https://doi.org/10.1016/j.jastp.2009.03.008.

Pilger, C., Ceranna, L., Ross, J.O., Le Pichon, A., Mialle, P., Garcés, M. A., 2015. CTBT infrasound network performance to detect the 2013 russian fireball event. Geophys. Res. Lett. 42 (7), 2523–2531. https://doi.org/10.1002/2015GL063482.

Pilger, C., Schmidt, C., Streicher, F., Wüst, S., Bittner, M., 2013. Airglow observations of orographic, volcanic and meteorological infrasound signatures. J. Atmos. Solar Terr. Phys. 104, 55–66. https://doi.org/10.1016/j.jastp.2013.08.008.

Rousselot, P., Lidman, C., Cuby, J.-G., Moreels, G., Monnet, G., 2000. Night-sky spectral atlas of oh emission lines in the near-infrared. Astron. Astrophys. 354, 1134–1150.

Smith, A.K., 2004. Physics and chemistry of the mesopause region. J. Atmospheric Sol.-terrestrial Phys. 66 (10), 839–857. https://doi.org/10.1016/j.jastp.2004.01.032.

Snively, J., 2013. Mesospheric hydroxyl airglow signatures of acoustic and gravity waves generated by transient tropospheric forcing. Geophys. Res. Lett. 40 (17), 4533–4537. https://doi.org/10.1002/grl.50886.

Waxler, R., Assink, J., 2019. Propagation modeling through realistic atmosphere and benchmarking. Infrasound Monitoring for Atmospheric Studies. Springer, pp. 509–549. https://doi.org/10.1007/978-3-319-75140-5_15.

Please cite this article as: T. Le Dû, P. Simoneau, P. Keckhut et al., Investigation of infrasound signatures from microbaroms using OH airglow and ground-based microbarometers, Advances in Space Research, https://doi.org/10.1016/j.asr.2019.11.026